V(III) Doped Nickel Oxide-Based Nanocatalysts for Electrochemical Water Splitting: Influence of Phase, Composition, and Doping on the Electrocatalytic Activity

Daniel Böhm[1,2], Michael Beetz[1], Christopher Kutz[1], Siyuan Zhang[4], Christina Scheu[4,5], Thomas Bein[1]* and Dina Fattakhova-Rohlfing[2,3]*

[1]Department of Chemistry and Center for NanoScience (CeNS), Ludwig-Maximilians-Universität München (LMU Munich), Butenandtstrasse 5-13 (E), 81377 Munich, Germany

[2]Institute of Energy and Climate Research (IEK-1) Materials Synthesis and Processing, Forschungszentrum Jülich GmbH, Wilhelm-Johnen-Strasse, 52425 Jülich, Germany

[3]Faculty of Engineering and Center for Nanointegration Duisburg-Essen (CENIDE), University of Duisburg-Essen, Lotharstraße 1, 47057 Duisburg, Germany

[4]Max-Planck-Institut für Eisenforschung (MPIE) GmbH & RWTH Aachen, Max-Planck-Straße 1, 40237 Düsseldorf

[5]Materials Analytics, RWTH Aachen University, Kopernikusstrasse 10, 52074 Aachen, Germany

ABSTRACT: Doped nickel oxide-based compounds attract great interest as very efficient and abundant catalysts and were thoroughly investigated as battery materials in the past. However, there is still no clear understanding of the role of dopants on the complex dynamic character of their chemical and potential driven transformations. We have developed a synthesis procedure enabling the controlled formation of nanosized nickel hydroxide and nickel oxide polymorphs substituted with vanadium(III) ions and further investigated their structure-activity correlation for electrochemical water oxidation. The work thereby primarily focuses on an in-depth structural characterization of the homogenously doped nanosized α- and β-$Ni(OH)_2$ polymorphs. It could be shown that concentrations of 10 at% V(III) and higher can effectively inhibit a spontaneous phase transformation known as chemical aging of the turbostratic α- to the more crystalline β-$Ni(OH)_2$ phase in neutral aqueous media. The Fe-impurity biased electrocatalytic activity determined for α-/β-$Ni_{1-x}V_x(OH)_2$ showed only a minor increase of 10 % OER activity for an 1 at% doped non-aged sample resembling the α-phase while a 5 at% V(III) doped sample chemically aged over 24 h led to a doubled OER activity versus the undoped reference which transformed to β-$Ni(OH)_2$ over that period of time.

INTRODUCTION

Hydrogen generated by energy from renewable sources is regarded as a potential clean energy carrier and storage medium for the future energy and mobility sector.[1-2] In addition, the generated "green" hydrogen can further be used as process feedstock to lower the environmental impact in industry and generate valuable chemicals.[3-4] Alkaline electrolysis has been in commercial use for decades and employs nickel-based electrocatalysts that exhibit some of the highest activity within the 3d metal group, in addition to their relatively low cost and great abundance in contrast to noble metal catalysts such as RuO_2 and IrO_2.[5-6]

Oxygen evolution reaction (OER) catalysts on the anode side are thereby required to promote the kinetically more demanding half-reaction of the overall water splitting reaction involving four proton-coupled electron transfer reactions and an O-O bond formation step.[7] In the recent years diverse nickel-based OER catalyst such as Ni-transition metal (TM) layered-double hydroxides [8-10], Ni-TM-phosphides (Ni-TM-P) [11-12] and micro- and nanostructured nickel-TM-oxide and -hydroxides [13-14] gained considerable attention due to their high catalytic activity and stability under alkaline OER conditions.[15] The outstanding performance of these catalysts is attributed to synergistic effects of nickel and neighboring transition metals as well as a result of nanosizing and -structuring leading to a significantly increased catalytic surface area or an increased share of exposed highly active crystal facets or coordination unsaturated edge-structures.[15] Among the transition metals investigated for doping nickel-based materials to date, iron was first reported by T. A. Edison in 1908 to influence the electrochemical behavior of nickel hydroxide used for alkaline storage batteries and studied in detail in 1987 by D. Corrigan concerning its influence on the OER activity of nickel oxide anodes.[16-17] Since then Ni-Fe based catalyst were intensively investigated due to their high performance, although the exact mechanism behind the extraordinary decrease in the OER overpotential (η_{OER}) as well as the structure and identity of the catalytically active site were still unclear. This has been attributed to the numerous difficulties arising from the complex structure-activity relationship in the nickel hydroxide structure.[8]

Recent studies revealed that even trace concentrations of transition metal ions, down to the parts per billion level in the electrolyte, have a tremendous effect on the OER activity of pure undoped $Ni(OH)_2$ anodes, which otherwise exhibit a low OER activity and rather high OER overpotential.[18-19] In-situ X-ray absorption spectroscopy analysis of Ni–Fe oxides together with density functional theory (DFT) calculations in the group of Bell have indicated that iron and not nickel is the active site for the catalytic reaction in the mixed-metal oxide films.[19-20]

However, the fact that pure iron (oxy)hydroxide films do not show a reasonable OER activity and that the performance of mixed NiFe catalysts reaches a maximum activity for ≈25 at% Fe level indicates that a surrounding NiOOH matrix is required for the dopant active sites.[20] It could be further shown by X-ray absorption spectroscopy and with cyclic voltammetry (CV) data that an initially present α-$Ni(OH)_2$ phase with nickel in oxidation state +II is transformed to a structurally similar Ni^{3+}-containing γ-NiOOH phase at elevated potential, representing an initial active phase for OER, which is in accordance with the phase transition model of $Ni(OH)_2$ first proposed by Bode et al. and extended by Mellsop et al..[20-22]

These findings highlight the importance of the initial $Ni(OH)_2$ phase as a second important factor determining the electrochemical properties of Ni-based catalysts, whose final structure can strongly vary depending on the synthesis conditions and chemical or electrochemical post-treatments. The α-$Ni(OH)_2$ phase is a layered brucite-type structure composed of Ni^{2+} ions bound to six octahedrally coordinated OH^- anions (each hydroxide being bonded to three nickel ions), with water molecules between the parallel layers.[19] It is further known that several forms of structural disorder exist, including stacking defects, different degrees of hydration and the incorporation of foreign anions resulting in a turbostratic structure.[23] An interesting and electrochemically relevant reaction for the nickel hydroxide is known as chemical aging, in which α-$Ni(OH)_2$ converts to a well-ordered β-$Ni(OH)_2$ phase with parallel-stacked layers accompanied by a removal of interlayer H_2O. Depending on the pH value, this process can proceed via either a dissolution/precipitation mechanism comparable to Ostwald-ripening, or a "zipper" model displacing interlayer H_2O molecules with hydroxide as the "teeth" on a nickel backbone.[24] Among other transition metal ions, doping with trivalent Al^{3+} was shown to significantly affect the stacking of $Ni(OH)_2$ layers during the aging process and thereby to stabilize the α-phase.[25-26]

In a recent work by Fan et al. the synthesis of highly OER active monolayers of vanadium (III) doped $Ni(OH)_2$ layered double hydroxide (LDH) of the α-$Ni(OH)_2$ phase was demonstrated, even outperforming similarly synthesized $NiFe(OH)_2$ LDH. The effect of V-doping on the catalytic activity and the complex nature of Ni-Fe active sites in $Ni(OH)_2$-based OER catalysts is still under investigation. The increased catalytic activity in the Ni(Fe)V-hydroxide system is thereby attributed to a modulation of the electronic structure of the Ni-Fe active sites to optimize the adsorption energies of OER reaction intermediates, an increased conductivity and an optimized nanomorophology.[8, 27] According to reports on the OER mechanism and activity of $Ni(OH)_2$ based OER catalysts under strict Fe-free environment, doping elements such as V(III) are not regarded as directly being part of the catalytically active sites but rather modulate the electronic structure of existing Ni-Fe active sites.[8, 27-29] J. S. Gon Gonçalves et al. thereby recently presented a literature overview of V-containing OER catalysts with identifying the key aspects responsible for an enhanced catalytic activity of various mixed vanadium oxides.[30] Besides being indirectly involved in the OER active sites, an optimized nanomorphology with an increased number of accessible active sites or the formation of defect rich $Ni(OH)_2$ phases are both expected to significantly influence the overall OER activity.[8]

To investigate such a structure-activity relationship of V(III) doped $Ni(OH)_2$, we have synthesized nanosized $Ni_{1-x}V_x(OH)_2$ with different degrees of V-doping to address the following questions: (i) whether the doping element vanadium is incorporated in the crystal structure and how it affects the morphology at the nanoscale; (ii) how V-doping influences the phase transformation of α- to β-$Ni(OH)_2$ phase during the chemical aging process (iii) how the altered phases and nanostructures of doped $Ni(OH)_2$ correlate with the catalyst performance towards the oxygen evolution reaction. V(III) was chosen as a doping element in this work as preliminary experiments with a series of transition metals (Co(II), Mn(II) Cr(III) and V(III)) showed a comparably strong effect on the phase transition of α- to β--$Ni(OH)_2$. Since small particle sizes below 10 nm [31-33] and a high degree of disorder [34-35] within the structure of nickel hydroxide are reported to positively influence the catalytic activity of the material as shown for recent examples of highly OER active nanostructured α-$Ni(OH)_2$ [36-38], we have modified a rapid aqueous oxidation method introduced by Sutto for the synthesis of various metal hydroxide nanoparticles [39] to obtain nanosized undoped and V-doped α-$Ni(OH)_2$.

RESULTS AND DISCUSSION

Structural characterization of time dependent phase transitions of undoped and V(III) doped NiOH2

Figure 1 depicts the synthesis approach used for the fabrication of pure and vanadium doped α- and β-$Ni(OH)_2$ polymorphs. Rapid oxidation of the aqueous Ni(II) / V(III) solution and quenching with MeOH under optimized reaction conditions (see supplementary information **Figure S1-4**) leads to the co-precipitation of an α-$Ni_{1-x}V_x(OH)_2{}^+Cl^-$ product whose color gradually shifts from turquoise and green to yellow for increased V(III) concentrations (Figure 1b). The transformation to the β-$Ni(OH)_2$ phase could be achieved by stirring the aqueous reaction product under ambient conditions, as revealed by X-ray diffractograms (XRD) (**Figure 2**a). Reaction products stirred and aged for up to 1 h (Figure 2a black curve) display broad reflections correlated with the α-$Ni(OH)_2$ phase (see zoom insets in Figure 2a for details), which gradually transforms to the β-phase with broad reflections visible after 3 h aging time (dark grey curve). The proposed models for this phase transition known as chemical aging are the ripening and zipper models, whereby the latter one is assumed to dominate at the given reaction conditions in deionized (DI) water.[24] Aging in DI water was chosen to avoid a simultaneous vanadium leaching possible under strong alkaline conditions which could alter the composition and thereby affect the process. The different broadening of the 100 and 101 reflection is thereby associated with a β-phase $Ni(OH)_2$ structure with defects in the layer stacking [35, 40], which increases in order by visibly sharpened reflections upon extended aging periods of 24 h (brownish curve) and 2 weeks (orange curve).

To effectively discriminate between α and/or β-phase $Ni(OH)_2$ we have used Raman spectroscopy, which is very sensitive towards structural variation induced by the degree of hydration, crystallinity or impurities in form of doping elements. Differently aged products (Figure 2b) indicate the presence of a $Ni(OH)_2$ phase by the strongly visible lattice vibrational mode at 450 cm^{-1} associated with both the α- (lattice mode) and β-phase (A_{1g} mode) [23]. With increasing aging time the α-phase associated 2nd order lattice vibrational mode at 1075 cm^{-1} [23] is reduced and not further visible in the spectra of the 24 h aged sample. In parallel with ongoing aging periods an increased intensity for the β-phase associated E_g mode is shown at ≈315 cm^{-1} as well as for the vibrational mode at 3581 cm^{-1} associated with surface OH, lattice/bulk OH and layer H_2O.[23] According to the Raman spectra and X-ray diffractograms, for up to 1 h aging, the pure α-$Ni(OH)_2$ is formed, which slowly undergoes a phase transition to β-$Ni(OH)_2$ by chemical aging in DI water within ≈24 h, with an intermediate product associated with an interstratified α/β-phase $Ni(OH)_2$ structure after 3 h aging.[24] The emerging β-phase $Ni(OH)_2$ structure for the 3 h aged samples thereby exhibits strong structural defects shown by respective XRD line broadening and the presence of α and β phase related Raman bands, which are associated with a disordered stacking sequence.[24]

Dynamic light scattering (DLS) (Figure 2c) shows no measurable signal for fresh (aged below 1h) $Ni(OH)_2$, as the product is strongly agglomerated and practically not dispersible. However, after 3 h aging in solution, nanoparticles in the range of ≈10-20 nm are detected, and for 24 h aged $Ni(OH)_2$ the particle sizes increase to ≈80 nm. The observed change in particle size indicates that XRD line broadening and sharpening upon aging are not solely based on stacking disorder as proposed Delmas et al. but may also originate from the nanosized morphology.[35]

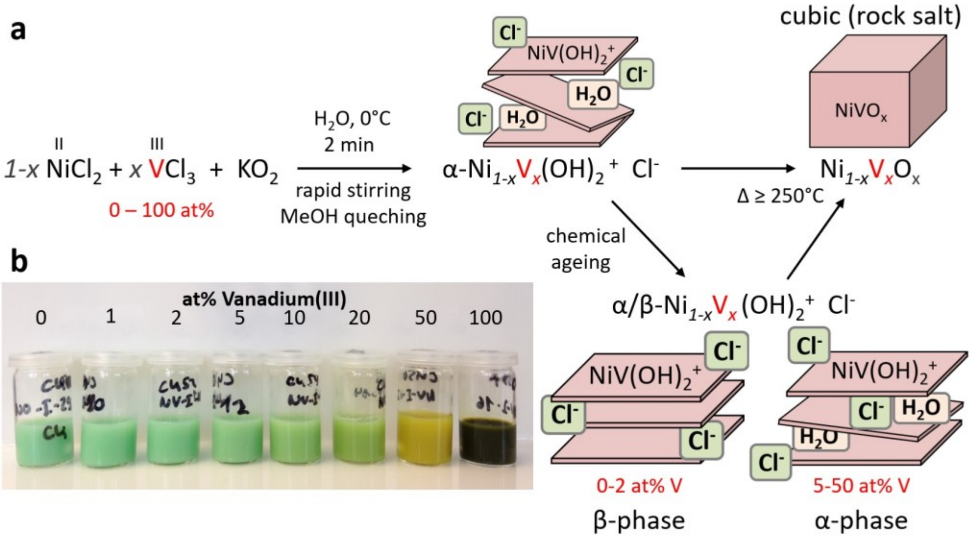

Figure 1 Schematic illustration of products prepared by the *α/β*-$Ni_{1-x}V_x(OH)^{2+}$ Cl^- synthesis route. (a) Schematic illustration of rapid co-precipitation by KO_2, phase transformation by chemical aging and calcination of $Ni_xV_{1-x}(OH)_2$. (b) Image of $Ni_{1-x}Vx(OH)^{2+}$ Cl^- product series with x∈[0;1].

To the best of our knowledge, morphological changes on the nanoscale from interstratified α-$Ni(OH)_2$ to β-$Ni(OH)_2$ nanoparticles were not reported in the literature so far, although β-$Ni(OH)_2$ nanoparticles in the range of 10-25 nm were observed but not specifically characterized as an aging product of α-$Ni(OH)_2$.[13] Further transformation to larger β-$Ni(OH)_2$ sheet-like structures with disordered stacking sequence upon chemical aging and transformation to an ordered β-$Ni(OH)_2$ phase are well described in the literature, including their properties as OER catalysts.[21, 41-43] The focus in most of the recent literature is thereby on the activity of specifically synthesized α- or β-phases featuring various nanostructures [13, 36-37, 44], however lacking a detailed investigation of the nanomorphology change during the chemical aging process and the effect of doping elements on this process. In this work, we therefore wish to address the question of how the addition of vanadium (III) ions in the synthesis influences the time-dependent phase transformation and morphological changes and to correlate these modifications with changes in OER activity.

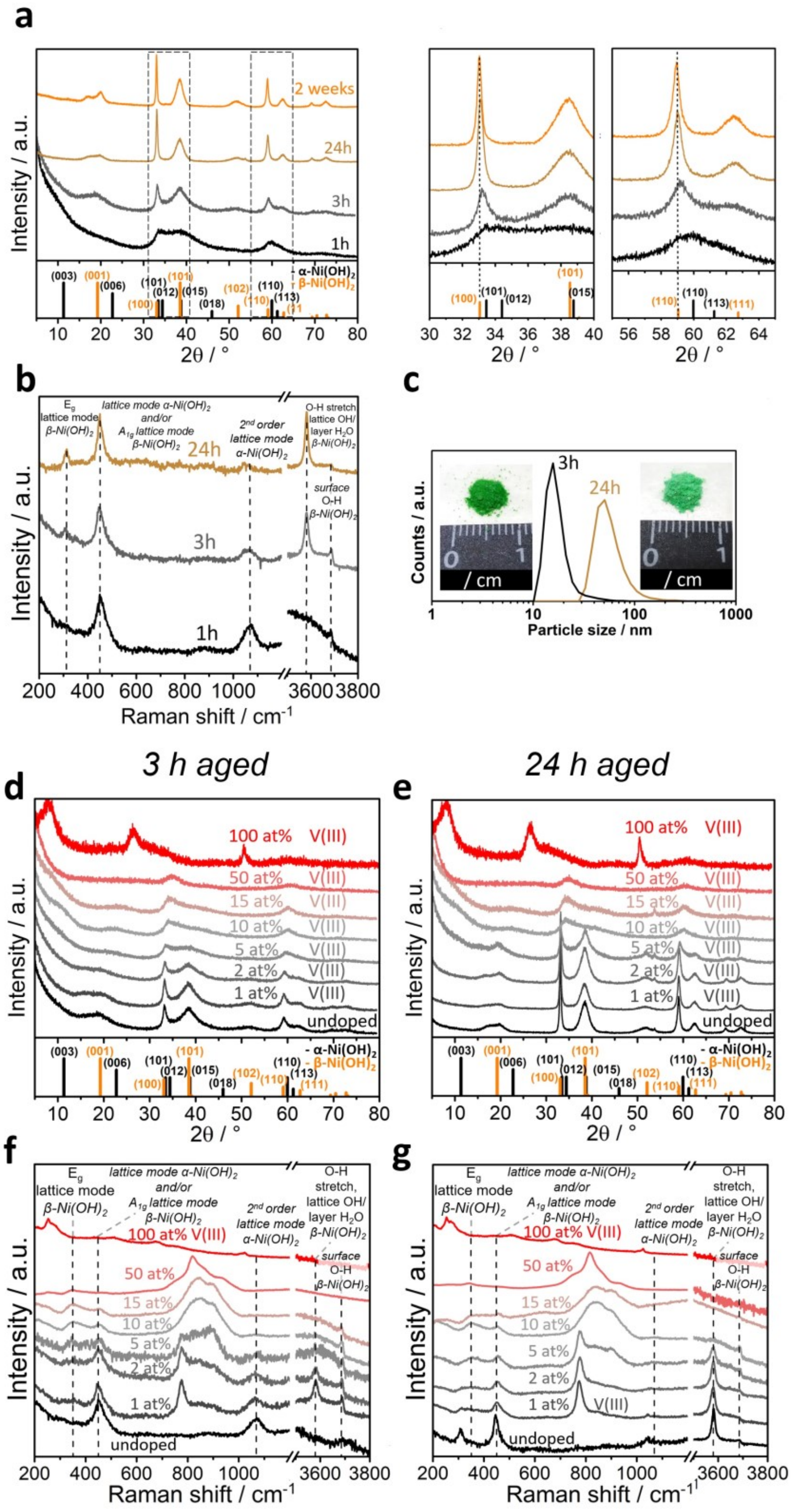

Figure 2 Structural characterization of time-dependent phase transitions of undoped and V(III)-doped NiOH$_2$ in aqueous solution (a) X-ray diffractograms of undoped Ni(OH)$_2$ after 1, 3, 24 h and 2 weeks of stirring of the aqueous reaction product mixture before drying. (b) Raman spectra of undoped Ni(OH)$_2$ after 1, 3 and 24 h of stirring of the aqueous reaction product mixture before drying. (c) Dynamic light scattering data of a diluted sample of undoped Ni(OH)$_2$ after 3 and 24 h of stirring of the aqueous reaction product mixture. X-ray diffractograms of a series of V(III)-doped Ni(OH)$_2$ (0-100 at% V(III)) after (d) 1 h and (e) 24 h of stirring of the aqueous reaction product mixture. α-Ni(OH)$_2$ (Ni(OH)$_2$ x 0.75 H$_2$O) pattern: ICDD card # 00-038-0715 (rhombohedral, a = b = 3.08 Å, c = 23.41 Å, α = β = 90°, γ = 120°). *β*-Ni(OH)$_2$ (Ni(OH)$_2$) pattern: ICDD card # 00-014-0117 (hexagonal, a = b = 3.126 Å, c = 4.605 Å, α = β = 90°, γ = 120°). (e) Raman spectra of a series of V(III)-doped Ni(OH)$_2$ (0-100 at% V(III)) after (f) 1 h and (g) 24 h of stirring of the aqueous reaction product mixture. The bands at 450 cm^{-1} (lattice mode) and 1070 cm^{-1} (2nd order lattice mode) are assigned to the α-Ni(OH)$_2$ phase.[23-24] Bands at 447 cm^{-1} (A$_{1g}$ lattice mode), 3581 cm^{-1} (O-H stretch / lattice OH / layer H$_2$O mode) and 3690 cm^{-1} (surface O-H stretch) were assigned to the *β*-Ni(OH)$_2$ phase.[24]

The addition of 2 at% V(III) results in the formation of a product with visibly altered crystallinity, as indicated by the broadened reflections in the respective diffractogram in Figure 2d for the ≈3 h aged doping series as compared to the undoped material (black curve). With increasing V(III) concentration, the reflections broaden significantly, which indicates a delayed aging process with increased stacking defects and small crystallite domain sizes. A successful doping of V(III) in the $Ni(OH)_2$ structure by the proposed rapid co-precipitation synthesis is indicated by a gradual shift of the 100 reflection at ≈34 °2-theta and 110 reflection at ≈60 °2-theta to higher angles in the concentration range of 0-50 at% V(III) due the slightly smaller ionic radius of V^{3+}(≈0.64Å)[45] vs. Ni^{2+}(0.69Å)[45]. Inductively coupled plasma – optical emission spectrometry (ICP-OES) measurements (Figure S1) of washed co-precipitation products furthermore confirmed the quantitative incorporation of vanadium ions over a range of 1-15 at%. Even for a 50 at% V(III) concentration in the precursor solution, ≈39 at% vanadium is incorporated in the reaction product without any visible side phase formation (as observed by XRD) (Figure 2d).

The presence of vanadium ions is visible in the Raman spectra of samples doped with as little as 1 at% V(III), with an additional band present at around ≈775 cm^{-1} attributed to a V-O vibrational mode, which was not reported in literature so far for doped $Ni(OH)_2$ but for nickel-vanadium mixed oxides.[46] With increasing vanadium content, a broad band at ≈845 cm^{-1} with a shoulder at ≈900 cm^{-1} arises. These may be attributed to vanadium oxide anions, which may form after the solubility limit of V^{3+} ions in $Ni(OH)_2$ is reached.[46-47] The insertion of vanadate anions into the interlayer space was described by Park et al..[48] This concentration-dependent increase of interlayer ion-associated bands is correlated with a decrease in intensity of the β-phase-associated band at 3581 cm^{-1}, suggesting a lower content of stacked $Ni(OH)_2$ sheets or β-$Ni(OH)_2$ particle size with surrounding α-phase.[24, 31] Doping concentrations of 50 at% V(III) in the precursor solution, corresponding to ≈39 at% V(III) content in the product (**Table S1**) show one dominant band at 850 cm^{-1}, besides broadened bands at ≈775 and ≈900 cm^{-1}. The difference in band intensities may thereby be explained by an altered amount of excitable inter- and intralayer V-O vibrations.

A chemical aging period of 24 h for the $Ni_{1-x}V_x(OH)_2$ series reveals a correlation between the V-doping concentration and the crystallization process over an intermediate nanocrystalline β-phase $Ni(OH)_2$ (3 h aged sample) with high stacking disorder to form the β-phase product (24 h aged sample) with increased stacking order. Doping concentrations as low as 2 at% V(III) (Figure 2e) significantly delay the ordering of $Ni_{1-x}V_x(OH)_2$ sheets, with concentrations from 10 at% V and higher fully preventing further crystallization as shown by matching diffractograms of 3 h vs. 24 h aged samples with respective concentrations. An inhibiting effect of V(III) ions on the β-$Ni(OH)_2$ crystallization and ordering by chemical aging is also visible in the Raman spectra of the differently aged doping series. The intensity of the band corresponding to the A_{1g} lattice mode at ≈450 cm^{-1}, corresponding to both α- and β-$Ni(OH)_2$ [23], is inversely correlated to the V(III) concentration as well as the band at 3581 cm^{-1}, which is associated with an O-H stretch / lattice OH and layer H_2O mode[23] observed for undoped β-phase $Ni(OH)_2$ (Figure 2b).

Electron microscopy and electron energy loss spectroscopy for the investigation of time dependent phase transitions and nanoscale morphology of undoped and V(III) doped $NiOH_2$

Time-dependent phase transitions induced by chemical aging were investigated in more detail by electron microscopy to correlate changes of the crystal structure analyzed by XRD and Raman spectroscopy to the nanoscale morphology and local structure of the material. **Figure 3**a-c confirms the amorphous and agglomerated structure of up to 1 h chemically aged $Ni(OH)_2$ as indicated above by XRD, Raman and DLS data. The electron diffraction pattern shows broad diffuse rings that are attributed to the presence of α-phase $Ni(OH)_2$. The crystallization of small nanoparticles in the range of 2-4 nm from the surrounding turbostratic α-phase (Figure 3d) for 3 h aged $Ni(OH)_2$ could be observed directly in high resolution TEM images (Figure 3e and inset) and was already proposed by DLS measurements (Figure 2c), with lattice spacings of single nanoparticles (**Figure S5**a) corresponding to the β-phase. In agreement with the XRD data, the electron diffraction results confirm the increase in crystallinity and transformation to well-stacked β-phase $Ni(OH)_2$ for 24 h aged $Ni(OH)_2$ (Figure 3i).

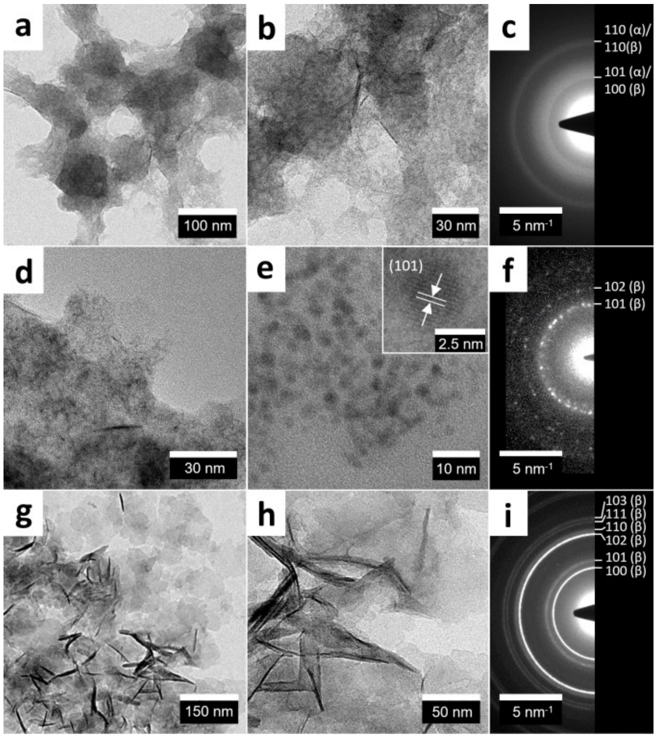

Figure 3 Structural characterization of time-dependent phase transformations by TEM of 1 h (a-c), 3 h (d-f) and 24 h (g-i) $Ni(OH)_2$ aged samples. TEM images of 1h aged $Ni(OH)_2$ (a, b) turbostratic phase with selected area electron diffraction pattern (c). TEM images of 3 h aged sample (d, e) with nanoparticle (e, and

inset) morphology and ED pattern (f). TEM images of 24h aged $Ni(OH)_2$ sample with nanosheet morphology and ED pattern (i). α-$Ni(OH)_2$ ($Ni(OH)_2 \cdot 0.75\ H_2O$) pattern: ICDD card # 00-038-0715. *β*-$Ni(OH)_2$ ($Ni(OH)_2$) pattern: ICDD card # 00-014-0117.

The visibly sharpened β-$Ni(OH)_2$ 101 reflection observed by XRD (Figure 2a) upon chemical aging suggests - besides a lower amount of defects in the layer stacking - a growth of the nanosized material along the crystallographic ac-plane that is directly observable in form of a nanosheet-like morphology and evident in the respective electron diffraction pattern (Figure 3i).

The microstructure of doped $Ni(OH)_2$ was investigated for 5 at% (**Figure 4**) and 10 / 15 at% (**Figure S6**) V-containing product chemically aged for ≈3 h and 24 h, respectively. 5 at% V-doped $Ni(OH)_2$ aged for 3 h depicted in Figure 4a, b resembles the nanoparticle-based morphology of undoped and equally long aged hydroxide depicted in Figure 3d, e. Although the crystallinity shown by XRD (Figure 2d) is lower than that of the undoped counterpart (Figure 2a), the electron diffraction pattern (Figure 3f and Figure 4c) indicate a similar β-phase $Ni(OH)_2$ structure with disordered stacking sequence.

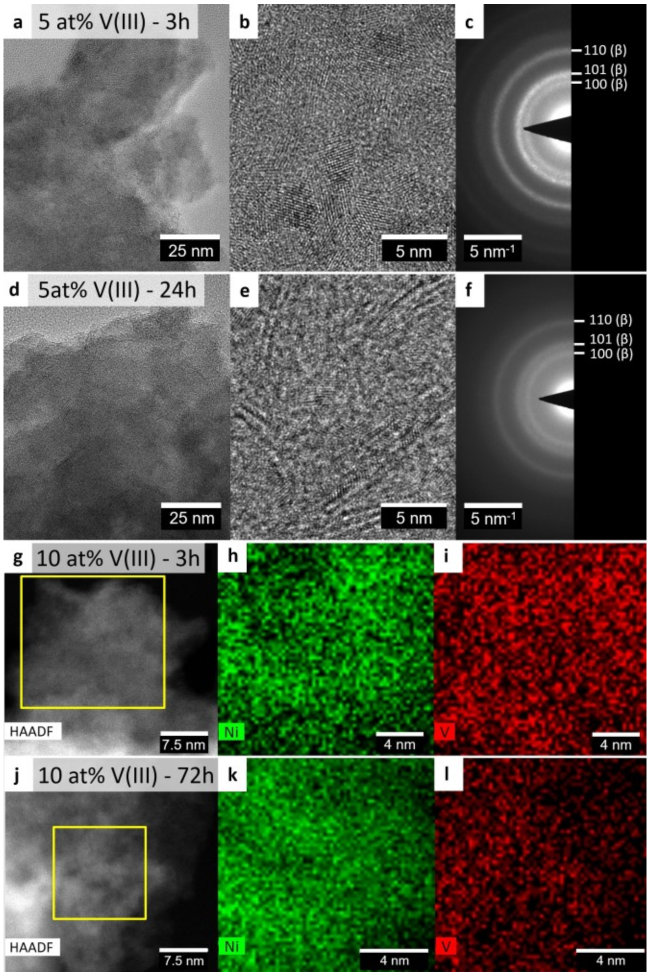

Figure 4 Structural characterization of time-dependent phase transformations of V(III) doped $Ni(OH)_2$ by TEM. TEM images and electron diffraction pattern of 5 at% V(III) doped $Ni(OH)_2$ after 3 h (a-c) and 24 h (d-f) aging time. *β*-$Ni(OH)_2$ ($Ni(OH)_2$) pattern: ICDD card # 00-014-0117. (g-l) STEM atomic-contrast micrographs and EDX elemental mappings of Ni and V.

An influence on the phase transformation process becomes evident for 5 at% doped samples chemically aged for 24 h. As suggested by the X-ray diffractograms in Figure 2d, e, vanadium doping strongly inhibits the crystallization and proper $Ni(OH)_2$ sheet stacking, which is illustrated by a comparison of the respective electron diffraction patterns (Figure 3i and Figure 4f). According to our TEM investigations, V-doping inhibits particle growth along the crystallographic *ac*-plane, as only short and stacked sheet-like structures are observable by TEM (Figure 4e) in contrast to tens of nanometer long well-defined sheets (Figure 3g, h) for equally aged undoped material. Higher concentrations of 10 and 15 at% V(III) in 3 h and 24 h aged samples (Figure S6a-f), respectively, show very similar nanostructures of particles (3 h aged) and small sheet-like fragments (24 h aged) in HR-TEM images.

ICP-OES measurements (Table S1) confirm that the V(III) contents in the $Ni_{1-x}V_x(OH)_2$ samples are very close to the nominal doping level of up to 15 at% V. STEM-EDX mapping measurements of 10 at% V-doped samples chemically aged for 3 h (Figure 4g-i) and 24 h (Figure 4j-l), further confirm the uniform distribution of V on the nanoscale (**Figure S7**a-f), as well as the micrometer-scale (Figure S7g-i).

It can be concluded that the rapid co-precipitation of the Ni(II) and V(III) precursor by KO_2 in aqueous solution leads to homogeneously doped α-$Ni_{1-x}V_x(OH)_2$ that undergoes a transformation to β-phase nanoparticles after ≈1-3 h and for low doping concentrations (up to ≈5 at%) a further assembly/growth of nanoparticles to sheet-like β-$Ni(OH)_2$ particles within 24 h without a detectable segregation of V(III) dopant. Higher V(III) concentrations ≥10 at% thereby inhibit the proper stacking required for the beta phase formation also with a 24 h aging duration.

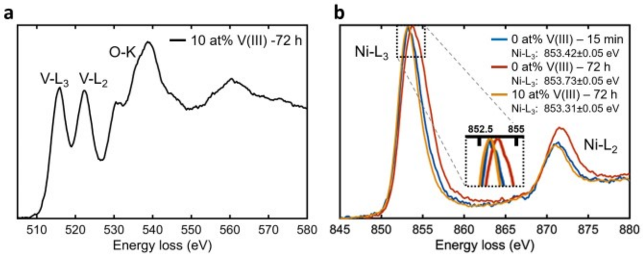

Figure 5 Structural characterization of time-dependent phase transformation of V(III) doped $Ni(OH)_2$ by EELS. (a) EELS spectrum with V-L_3, V-L_2 and O-K edge of 10 at% V(III) doped $Ni(OH)_2$ sample after 72 h aging. (b) Overlay of EELS spectra in energy loss region of Ni-L_3 and Ni-L_2 edge of $Ni(OH)_2$ samples after 15 min (blue curve), 72 h (orange curve) aging, and 10 at% V(III) doped $Ni(OH)_2$ samples after 72 h aging (yellow curve).

To further investigate the influence of V(III) doping on the phase transformation upon chemical aging, electron energy loss (EELS) spectra (**Figure 5** and **Figure S8**) were recorded. As shown in Figure 5b, Ni-L_3 and Ni-L_2 edges of α-$Ni(OH)_2$ (15 min) and α-$Ni_{0.9}V_{0.1}(OH)_2$ (72 h) are at very similar positions. In contrast, the edges of β-$Ni(OH)_2$ (72 h) shift towards higher energy loss. The so-called chemical shift is caused by a shift in the unoccupied states with respect to the core states (2p for L_2 and L_3 edges), which may indicate changes in the valence state and the local coordination of the present phase.[49] For example, there is a clear peak shift of ≈0.3 eV between α- and β-$Ni(OH)_2$. On the other hand, the introduction of 10 at% V(III) hardly changes the chemical shift of the α-like $Ni_{0.9}V_{0.1}(OH)_2$. The calculated electronegativity (dimensionless values according to the Pauling scale) values of Ni^{2+} and V^{3+} are χ_i = 1.367 [50] and χ_i = 1.545 [50], respectively. A shift of the Ni-L_3 edge due to a partial oxidation of Ni^{2+} may not be ruled out, but clearly plays a lesser role. The EELS measurement serves as further evidence for a V(III) induced inhibition of the phase transformation and stacking of turbostratic α-$Ni(OH)_2$ to the well stacked β-$Ni(OH)_2$ under given synthesis conditions.

Oxygen evolution reaction catalysis performance of chemically aged $Ni_{1-x}V_x(OH)_2$

The electrochemical performance of chemically aged $Ni_{1-x}V_x(OH)_2$ towards the oxygen evolution reaction was measured for thin film samples in a diluted KOH electrolyte (see experimental part for sample preparation and exact measurement conditions) with potential trace impurities of Fe ions. SEM images of prepared electrodes of 1 h and 24 h aged product reveal an aggregated particle-like morphology and a smoother sheet containing (indicated by red arrows in **Figure S9**d) morphology, respectively.

In the cyclic voltammograms, α-phase electrodes (**Figure 6**a and **Figure S10**a) show a pronounced Ni^{2+}/Ni^{3+} redox feature centered around 160 mV with respect to theoretical oxygen evolution reaction potential of 1.23 V vs. reversible hydrogen electrode (RHE) and referenced as η_{OER}. The Ni^{3+} oxidation peak located at η_{OER}≈250 mV in the first cycle with a marked shift to η_{OER}≈175 mV for later cycles is attributed to the α-γ phase transformation as proposed in the literature.[22, 51-52] The shift of the oxidation peak to lower potentials within the first cycles is thereby assumed to result from a restructuring of the initial anodic $Ni(OH)_2$ layer.[22] Upon cycling (the 4th vs. the 20th cycle) the Ni^{2+}/Ni^{3+} redox feature slightly decreases accompanied by an increase in OER activity, which is explained by a quasi-reversible formation of the catalytically active γ-NiOOH phase, as widely accepted in the literature.[21-22, 38]

In comparison, aged β-$Ni(OH)_2$ phase (Figure 6b and Figure S10b) does not show a visible reduction to Ni^{2+} during CV cycling, but a Ni^{3+} oxidation feature that is η_{OER}≈50 mV further positive centered at η_{OER}≈300 mV than for the α-phase product. During cycling this Ni^{2+}/Ni^{3+} oxidation feature is analogously lowered to η_{OER}≈225 mV, which is ≈50 mV higher than for the α-phase. The oxidation peak is thereby associated with a less reversible β-$Ni(OH)_2$ to β-NiOOH transformation and in agreement with the structural characterization of the 24 h aged $Ni(OH)_2$ product.[22, 51-52]

In terms of the OER activity, the turbostratic α-phase product (0 at% V – 1 h aged) (Figure 6e) shows, with ≈34.5 mA cm^{-2}, more than 4 times the activity as compared to ≈6.8 mA cm^{-2} for the 24 h aged β-phase $Ni(OH)_2$ (0 at% V – 24 h aged) (Figure 6f), with both values being determined for the 20th CV scan cycle at an OER overpotential of 400 mV. The overpotentials required to reach an OER current density of 10 mA cm^{-2} were calculated to be ≈340 mV and ≈432 mV for the 1 h and 24 h aged sample, respectively. In comparison, α-Ni(OH)2 OER catalysts reported by Luan et al. exhibit an OER overpotential of 260-320 mV depending on the morphology with highest performance obtained for a nanoparticle based catalyst.[38] A further example of an optimized OER catalyst was reported by Zhang et al. who synthesized an α-$Ni(OH)_2$-nanosheet catalyst on nickel foam substrate that showed an η_{OER} of 266 mV.[37] The limited OER activity of our prepared catalyst samples compared to literature reports is attributed to the non-optimized electrode morphology in form of densely coated, micrometer thick (see Figure S9) and relatively poor conductive hydroxide layers deposited simply by drop-casting. Together with a non-optimized nanomorphology a comparably low electrochemically active surface area is expected which further lowers the performance.

The effect of vanadium (III) doping on the cyclic voltammograms of 1 h aged $Ni(OH)_2$ (Figure 6c and **Figure S11**a) is a significantly broadened Ni^{2+}/Ni^{3+} oxidation feature beginning around η_{OER}=150 mV and ranging up to the OER potential depending on the doping concentration. The low potential part of the feature thereby indicates the presence of α-$Ni(OH)_2$, which undergoes the α-γ phase transformation.[22, 51-52] The broadening of the oxidation peak enhanced for higher doping concentrations is further regarded to result from a restructuring of the initial anodic $Ni(OH)_2$ layer that is still observable after 20 scan cycles, as opposed to the undoped α-phase product where this process is completed within the first 2-3 scan cycles (see Figure 6a). The OER activity of the 1 h aged sample shows a maximum of ≈38.1 mA cm^{-2} for 1 at% V-doped sample (Figure 6e and **Table S2**) and a decrease directly correlated to the doping ion concentration.

In comparison, 24 h chemically aged $Ni_{1-x}V_x(OH)_2$ shows a lower and anodically shifted Ni^{2+}/Ni^{3+} redox feature as observed for equally aged undoped $Ni(OH)_2$, indicating a β-$Ni(OH)_2$ to β-NiOOH transformation for doping concentrations below 10 at% V(III). Higher doping concentrations lead to a cathodic shift of the oxidation feature onset by ≈50 mV, which we attribute to a partial contribution by a α-γ phase transformation (Figure 6d and Figure S11b). According to the voltammograms it can be concluded that 24 h aged $Ni(OH)_2$ doped with ≥10 at% V(III) shows characteristics of a α/β-$Ni(OH)_2$ mixed or interstratified phase.

The OER activity (Figure 6f and **Table S3**) exhibits a maximum at a V(III) concentration of 5 at%, which results in an approximately doubled (≈14.6 vs. ≈6.8 mA cm^{-2} at η_{OER}=400 mV, 20th scan cycle) catalytic performance for the doped sample.

The discrepancy between the V(III) ion concentrations of catalytically most efficient 1 h and 24 h aged samples indicates that the structure/morphology of $Ni(OH)_2$ modified by the doping is the reason for the altered OER activity, which is in agreement with literature reports on the electrocatalytic activity of different $Ni(OH)_2$ phases [22, 37] and active center sites.[38] It has to be emphasized that not the doping element vanadium is regarded to be part of the active sites and directly involved in the OER but it mainly account for structural/morphological changes that make the Ni-Fe active sites developed in the non-Fe free environment more accessible. By this mechanism the V(III) doping indirectly influences the initial OER activity which was investigated in this work and correlated to the structure.

Structural characterization and OER catalysis performance of calcined $Ni_{1-x}V_xO$

With a series of V(III) doping concentrations, the phase transformation from hydroxide to the rock-salt $Ni_{1-x}V_xO$ structure upon calcination was investigated. For the 1 h aged $Ni(OH)_2$ sample with α-phase structure a transition temperature of ≈275°C was measured by thermogravimetric analysis with differential scanning calorimetry (**Figure S12**a).

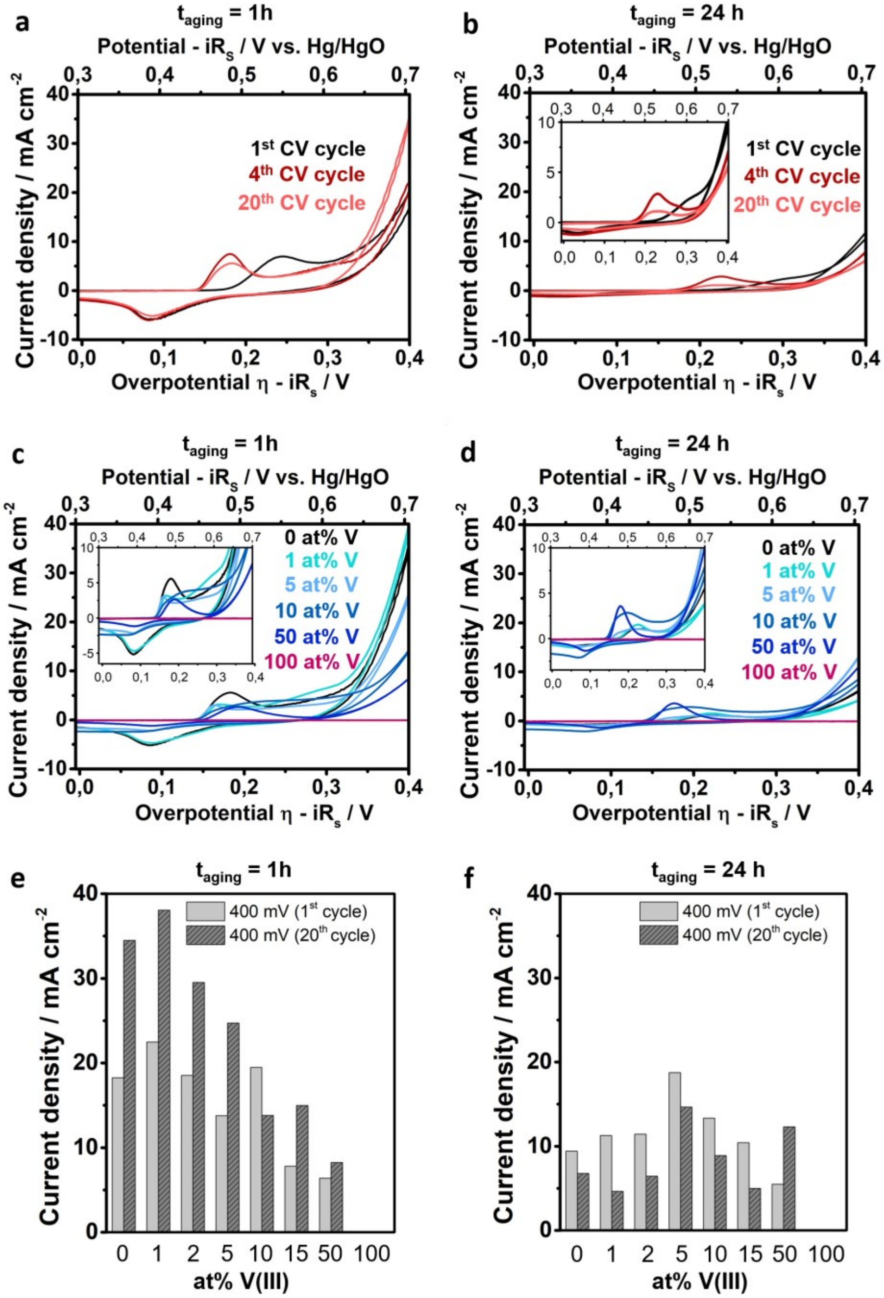

Figure 6 Electrochemical characterization of chemically aged and V(III) doped $Ni(OH)_2$. Cyclic voltammograms (1st, 4th and 20th scan cycle) of 1 h (a) and 24 h (b) aged undoped $Ni(OH)_2$. (c) Cyclic voltammograms (20th scan cycle each) of 1 h (c) and 24 h (d) aged 0, 1, 5, 10 and 50 at% V(III) containing $Ni(OH)_2$ (nominal doping concentration) and 100 at% V(III) based sample. Plot of OER activities of V(III) containing $Ni(OH)_2$ at an overpotential of 400 mV for the 1st and 20th CV scan cycle for 1 h (e) and 24 h (f) chemically aged samples. Mass-loading on FTO substrate electrodes ~50µg cm^{-2}.

For the undoped $Ni(OH)_2$ a calcination temperature of 250 °C was applied to obtain a nanosized product that can be assigned to the NiO rock salt phase with a further growth of crystalline domain sizes at higher calcination temperatures of up to 450 °C (Figure S12b). In comparison, for the 24 h aged β-phase $Ni(OH)_2$ product an increased phase transition temperature of close to 300 °C was measured (Figure S12c).

As the applied temperature range of 250-300 °C is below or very close to literature reported nickel hydroxide-oxide phase transition temperatures of ≈285 °C[53] for α-$Ni(OH)_2$ and ≈315-325 °C[53-54] for β-$Ni(OH)_2$, presumably a distorted nanosized NiO rock salt phase with residual water content is formed as reported in literature for similarly low calcination temperatures and indicated by a the broad NiO 111 and 200 reflex.[55]

XRD patterns of 300 °C and 250 °C calcined samples of 1 h aged $Ni_{1-x}V_xOH$ (**Figure 7**a and **Figure S13**b, respectively) reveal an inhibited growth of crystalline domains with increasing V(III) content, based on significantly broadened peaks and thermogravimetric analysis (Figure S13a). The phase transition temperature of 1 h aged $Ni_{0.9}V_{0.1}O$ is increased by ≈+50 °C versus the equally prepared undoped α-$Ni(OH)_2$.

The hydroxide to rock salt $Ni_{1-x}V_xO$ transformation (Figure S13a) is regarded to originate from a different degree of stacking disorder and interlayer H_2O in the hydroxide phase caused by vanadium doping. Even at higher calcination temperatures of up to 450 °C, V(III) doping levels of 10 at% significantly decrease the crystalline domain size as indicated by respective peak broadening (Figure S13c).

Possible ways to tune the crystallinity are therefore altering the calcination temperature (Figure 7b, c) or the doping level.

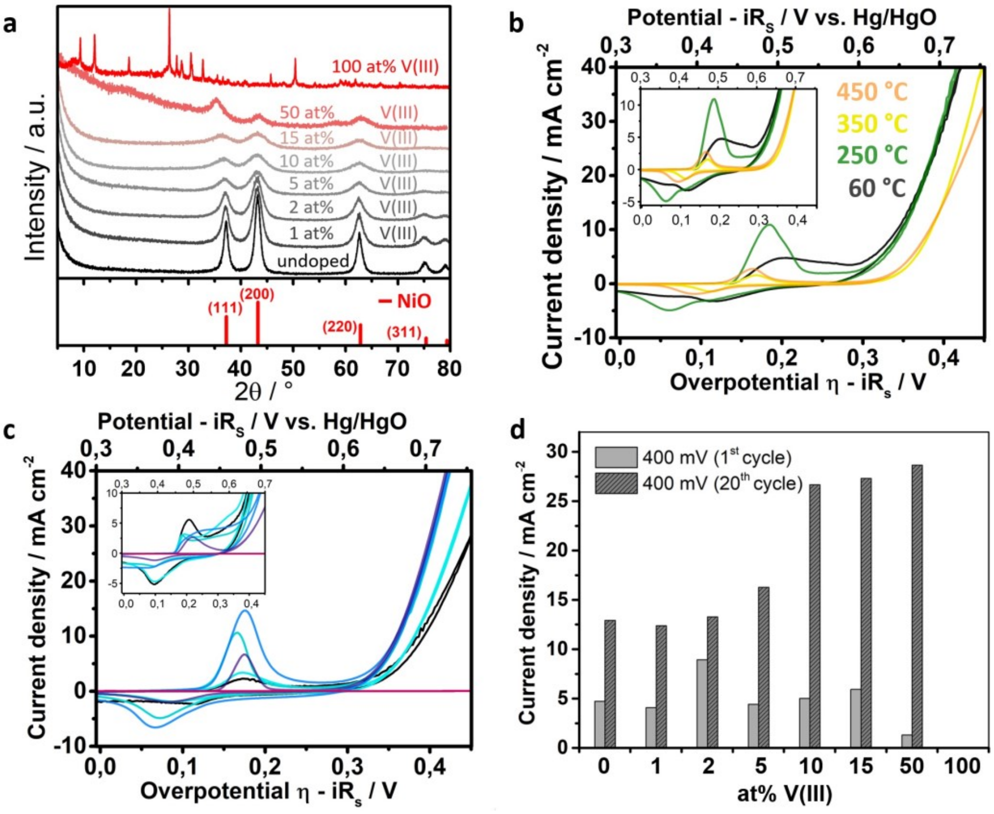

Figure 7 Characterization of structure and electrochemical activity of V(III)-doped $Ni(OH)_2$ after calcination. (a) X-ray diffractogram of 300 °C calcined V(III) doped $Ni(OH)_2$ (0-50 at% V(III) black and greyscale). (b) Cyclic voltammetry (20th scan cycle each) of 1 h aged 60 °C dried (black), and heated at 250 °C (green), 350 °C (yellow) and 450 °C (orange) $Ni_{0.9}V_{0.1}O_x$. (c) Cyclic voltammetry (20th scan cycle each) of 300 °C calcined $Ni(OH)_2$ with doping concentrations ranging from 0 (black), 5 (light turquoise), 10 (turquoise), 15 (blue), 50 (dark-violet) and 100 at% (violet) V(III). (d) Plot of OER activities of V(III) containing (0-100 at% V), 300°C calcined $Ni(OH)_2$ at an overpotential of 400 mV for the 1st and 20th CV scan cycle. Mass-loading on FTO substrate electrodes ~50µg cm^{-2}.

Calculated crystalline domain sizes of the rock salt structure according to Scherrer's equation derived from XRD signal broadening reveal a continuous decrease from ≈4.5 nm for undoped down to ≈2 nm for 10 at% V-doped samples calcined at 250 °C (Figure S13d, black data points). Analogously, samples calcined at 300 °C show domain sizes ranging from ≈8.5 nm for undoped NiO down to ≈2.5 nm for 15 at% V(III) doped $Ni_{1-x}V_xO$ (Figure S13d, red data points). Along with the decrease of crystallinity due to doping ions, an increase of the lattice parameter from ≈4.185 Å (undoped – 300 °C calcined) to ≈4.205 Å (≥10 at% – 300 °C calcined) determined from fitted reflection centers of X-ray diffractograms can be observed (Figure S13e and **Table S4**). Calculated lattice parameters linearly rise between 0 and 2 at% V, leveling off at 5 at% and reaching a maximum for 10 at% doping. The lattice parameters are larger than for rock salt NiO (4.178 Å, ICDD #01-071-1179) and are associated with a NiO_x phase containing hydroxyl group residues not fully transformed to the stoichiometric NiO rock salt phase within that temperature range.[56] Increased V(III)-ion doping that was shown to reduce the crystalline domain size is therefore regarded to lead to increased amounts of hydroxyl group residues enlarging the resulting crystallographic unit cell upon calcination at moderate temperatures of 300 °C. This hypothesis is supported by the formation of a hydrated NiO_x phase with even larger lattice parameters ranging from 4.27 - 4.30 Å (depending on the doping level) for a decreased calcination temperature of 250 °C (Figure S13e and **Table S5**).

Strikingly, even for high V(III) precursor concentrations of 50 at% resulting in a doping level of ≈39 at% (Table S1) no additional phases originating from V_2O_3, VO_2 or V_2O_5 can be observed at calcination temperatures of up to 300 °C. At even higher calcination temperatures of 450 °C for a $Ni_{0.9}V_{0.1}OHx$ sample no phase separation could be detected (Figure S13c). The high solvation limit of V(III) in the NiO_x phase, significantly exceeding the proposed limit of 5-10 at% V(III) by Park et al., may be attributed to a stabilization effect for nanoscale phases, as described by Fominykh et al. for Fe- and Co-doped NiO.[14, 57] Above the solubility limit, vanadium ions are not further incorporated into the $Ni(OH)_2$ lattice and result in a colored supernatant after washing of the synthesis product that is discarded.

Electrodes calcined at 250 °C (**Figure S14**) and 300 °C were investigated regarding their electrocatalytic activity with focus on the influence of their doping level. Calcination of 1 h aged α-$Ni(OH)_2$ $Ni_{0.9}V_{0.1}O_x$ product to 250 °C leads to a significant increase of the Ni^{2+}/Ni^{3+} redox feature with an accompanied shift of the oxidation feature from η_{OER}≈200 mV to η_{OER}≈175 mV.

The activity of the 250 °C calcined sample determined after 15 scan cycles thereby remained comparable to that of the hydroxide-based sample (Figure 7b) with a Tafel slope even outperforming both the unheated α- and β-phase product (**Figure S15**).

The cyclic voltammogram of V(III) doped $Ni_{1-x}V_xOH$ calcined at 300 °C shows a strong increase of the Ni^{2+}/Ni^{3+} redox feature for up to 10 at% doped samples, which is attributed to the decreased crystallite domain size and thus increased accessible active sites. An even higher V(III) content leads to a reduction of the redox feature, as the doping ion is shown to be redox inactive in the scanned potential range (see 100 at% V in Figure 7c).

Concerning the electrocatalytic activity for the oxygen evolution reaction, samples with 10-50 at% V(III) content show the best performance with up to ≈27.5 mA cm^{-2} among the 300 °C calcined samples (Figure 7d). The discussed effects of V-doping on the $Ni(OH)_2$ to NiO phase transition and resulting crystallite domain sizes upon calcination thereby explain the high catalytic activity of nanosized nickel-vanadium-oxide based OER catalysts upon calcination at temperatures up to 300 °C. For even higher calcination temperatures of 350 and 450 °C, a decrease in intensity of the Ni^{2+}/Ni^{3+} redox feature is observed with a further shift of the oxidation feature to η_{OER}≈150 mV accompanied by a significant decline of catalytic activity (Figure 7b).

CONCLUSION

Employing in-depth structural characterization, we have demonstrated that the rapid co-precipitation of nickel (II) and vanadium (III) chloride by potassium superoxide under cooling is a suitable synthesis approach for obtaining homogeneously doped α-$Ni(OH)_2$. Chemical aging by stirring of the reaction product in DI water - a known route for the conversion of α- to β- phase [24, 58] - is strongly inhibited by V(III) ions. Samples from 5 at% V(III) and higher thereby show a delayed transformation to a $Ni(OH)_2$ β-phase product with stacking disorder within 24 h, with samples of 10 at% V-content and higher structurally resembling the initial turbostratic α-phase. Foreign ion incorporation in the α- or β-phase $Ni(OH)_2$ has been reported for a variety of transition metal ions, and results for most in a slightly distorted Ni(OH)2 structure [25-26, 40] as also shown in this work. We attribute the inhibiting effect on the phase transition to the presence of vanadium ions in the structure that prevent the formation of larger $Ni(OH)_2$ nanosheets. These sheet-like structures can stack for low doping concentrations (<5 at%) according to proposed models [21, 24] and form β-Ni(OH)2 with a higher (doped samples) or lower (undoped samples) content of stacking defects.

Regarding the electrochemical activity towards the oxygen evolution reaction, it could be shown that a very low V-doping content of 1 at% can enhance the activity of α-phase related 1 h aged $Ni(OH)_2$ by ≈10 % to ≈37.5 mA cm^{-2} (η_{OER}=400 mV). The catalytic performance of chemically aged product resembling the β-phase $Ni(OH)_2$ on the other hand is generally lower by a factor of ≈3 (≈7.5 mA cm^{-2} for undoped, 24 h aged $Ni(OH)_2$), but can be doubled to ≈15 mA cm^{-2} by 5 at % V-doping. We attribute this minor enhancement for the 1 h short aged product to the fact that already the undoped product resembles the highly disordered α-phase, which is reported to be electrocatalytically more active than the ordered β-phase.[37-38, 44] The increase in activity for the V-doped and chemically aged samples is more pronounced due to the difference in crystallinity and phase. For these samples, a higher V(III) content effectively prevents a transformation to the ordered and stacked β-phase $Ni(OH)_2$. Vanadium doping in this synthesis procedure is therefore regarded to enhance the OER activity not as part of the active centers which are regarded to be Ni-Fe based in the Fe trace ion containing environment but indirectly by its influence on the crystallization upon chemical aging. The resulting structure and nanomorphology greatly affects the number of accessible active sites and therefore alters the overall OER activity of the doped material.

Further evidence for this hypothesis is obtained by the analysis of calcined $Ni_{1-x}V_x(OH)_2$. Again, V-doping can be directly correlated to a decreased crystallization or crystalline domain growth of $Ni_{1-x}V_xO$ in the cubic rock-salt structure. Here, even higher doping concentrations of up to 50 at% enhance the OER activity of given samples from ≈12 mA cm^{-2} to ≈27.5 mA cm^{-2} although the pure vanadium oxide was shown to be redox inactive in the applied potential range.

EXPERIMENTAL SECTION

1. Synthesis of (vanadium-doped) nickel-hydroxide polymorphs

The synthesis of undoped and vanadium doped nickel-hydroxide polymorphs is based on a rapid aqueous oxidation method introduced by Sutto[39].

For the synthesis of different nickel-hydroxide polymorphs per reaction 1.125 mmol nickel (II) chloride (SIGMA-ALDRICH, 98%) was dissolved in 7.5 mL bidistilled water (Millipore Q grade) to obtain a 0.15 M solution which was stirred for 1 h in air at room temperature. For vanadium doped $Ni(OH)_2$ samples vanadium(III)chloride (SIGMA-ALDRICH, 97%) was added to the solution to obtain a final concentration of 1, 2, 5, 10, 15, 50 at% vanadium and further stirred for 1 h for complete intermixing. Subsequently the precursor solution was cooled with an ice bath and 2.25 mmol potassium superoxide powder (KO_2, ABCR, 96.5% purity) was slowly added to the solution within 15 seconds under continuous stirring and quenched after 2 minutes by addition of 3.75 mL of precooled methanol (analytical grade). Amorphous α-$Ni(OH)_2$ was obtained as a powder after washing and evaporation of the solvent on a hot plate at 60 °C for 30 minutes and further drying in a laboratory oven in air at 60 °C for 16 hours. Ultrasmall β-$Ni(OH)_2$ nanoparticles were obtained as a powder in the same way, while the stirring time after the washing step was prolonged to 3 hours. After a stirring time of 24 hours, plate-like β-$Ni(OH)_2$ nanoparticles were obtained in the above-described way. During that stirring period, a color change from dark to light turquoise could be observed. The product was not obtained as a powder after evaporation of the solvent, but as a film on the glass slide. It had a brighter color compared to the α-$Ni(OH)_2$ powder after the film was scraped off and homogenized in a mortar.

2. Synthesis of (vanadium-doped) nickel-oxide powder

Dried samples obtained from the synthesis of undoped and vanadium doped Nickel-hydroxide were heated in a laboratory oven (NABERTHERM, model N15/65SHA) at 250 °C and 300 °C in air with a ramp time of 2 h and a dwell time of 2 h.

3. (V-doped) $Ni(OH)_2$ and NiO electrode preparation

Thin films of the catalytic layer were prepared by drop-casting a diluted dispersion of the wet pellet of nickel hydroxide onto FTO (fluorine-doped tin oxide, TEC15 substrates, DYESOL, Australia) or on quartz crystal microbalance (QCM) substrates. FTO substrates were cleaned with an aqueous solution of alkaline cleaner Extran (MERCK MILLIPORE), bidestilled H_2O and acetone. To enhance the hydrophilic properties of the surface, substrates were oxygen plasma-cleaned (Femto oxygen plasma surface cleaner, DIENER ELECTRONIC) prior to the drop-casting procedure. A Teflon-coated glass fiber tape leaving an exposed area of 0.159 cm^2 was used for masking. To precisely determine the mass loadings of equally prepared FTO electrodes, 0.5-inch Au-coated QCM sensors (KVG 10 MHz QCM device with gold electrode, Quartz Crystal Technology GmbH) were acetone cleaned, equally prepared and drop-casted with the catalysts according to the method employed for the FTO substrates. Dispersions with a concentration of ≈2 mg mL^{-1} were prepared by mixing 0.2 mL stock solution (wet pellet after last washing step in 3.5 mL H_2O) with 2.8 mL MilliQ H_2O. To reach a mass loading of ~50 µg cm^{-2}, 4 µL of the dispersion were deposited 1-4 times on a masked (0.159 cm^2) substrate, intermediate-dried on a hot plate at 50 °C, and completely dried for 16 h at 60 °C in a laboratory oven. (V-doped) nickel-oxide electrodes were fabricated by calcination of substrates at temperatures of 250 °C and 300 °C with a heating ramp of 2 h and a dwell time of 2 h.

4. Physico-chemical characterization

Wide angle X-ray diffraction analysis was carried out in transmission mode using a STOE STADI P diffractometer with Cu $K_{\alpha 1}$ radiation (λ = 1.54060 Å) and a Ge(111) single crystal monochromator equipped with a DECTRIS solid state strip detector Mythen 1K. Powder XRD patterns of the samples were collected with an omega-2theta scan in the 2θ range from 5° to 90° with a step size of 1° and fixed integration time of 25-35 seconds per step and a resolution of 0.05°. The size of crystalline domains of β-$Ni(OH)_2$ nanoparticles was calculated from line broadening of the 101 reflection with Scherrer's equation and XRD reference pattern for the β-$Ni(OH)_2$ phase (ICDD card number 00-014-0117: hexagonal, a = b = 3.126 Å, c = 4.605 Å, $\alpha = \beta = 90°$, $\gamma = 120°$).

Raman spectroscopy was carried out using a LabRAM HR UV-Vis (HORIBA JOBIN YVON) Raman microscope (OLYMPUS BX41) with a SYMPHONY CCD detection system and a He-Ne laser (λ = 633 nm). Spectra were recorded using a lens with a 10-fold magnification in the range from 100 cm^{-1} to 1000 cm^{-1} with filters of OD 0.3 - 0.6. Spectrum accumulation mode was used with integrating 600 times 30 sec per spectrum. The data acquisition was carried out with LabSpec software.

Transmission electron microscopy (TEM) specimens were prepared from nanoparticles in a 1:1 (v/v) ratio of water to ethanol solution and deposited on a carbon-film coated copper grid and dried in air. High resolution TEM, scanning TEM (STEM) images as well as electron diffraction patterns were recorded using two FEI Titan Themis microscopes with aberration correction of the probe-forming lenses operated at 120 kV or 300 kV. Energy dispersive X-ray spectroscopy (EDX) was performed using a SuperX windowless, four quadrant Silicon drift detector with a solid angle of 0.7 sr. Electron energy loss spectra (EELS) were acquired by a Gatan Quantum ERS spectrometer, collecting electrons scattered up to 35 mrad. Dual EELS acquisition enabled a reliable determination of the edge onset of Ni-L_3. Multivariate statistical analysis [59] was performed on the spectrum imaging datasets to reduce the noise.

SEM images were obtained with an FEI Helios Nanolab G3 UC scanning electron microscope equipped with a field emission gun operated at 3-5 kV. Specimens were prepared from nanoparticles in a 1:1 (v/v) ratio of water to ethanol solution and deposited on FTO or Si substrates that were glued onto a stainless-steel sample holder with silver lacquer. EDX measurements were performed at an operating voltage of 20 kV with a X-Max^N Silicon Drift Detector with 80 mm^2 detector area (OXFORD INSTRUMENTS) and AZTec acquisition software (OXFORD INSTRUMENTS).

5. Electrochemical characterization

For electrode preparation, dispersions with a concentration of around 2 mg mL^{-1} were produced by mixing 0.2 mL stock solution (wet pellet in 3.5 mL H_2O) with 2.8 mL MilliQ H_2O, stirred for 10 minutes at 500 rpm and sonicated for ≈ 30 minutes. To reach a mass loading of ~50 µg cm^{-2}, 4 µL dispersion was deposited on a plasma-cleaned FTO substrate or Au-coated QCM sensors (14 mm, 5 and 10 MHz AT-cut Cr/Au crystals from KVG QUARTZ CRYSTAL TECHNOLOGY GMBH and QUARTZ PRO AB) before drying on a hot plate at 50 °C. Electrodes were masked with PTFE tape to leave a circular electrode area of 0.196 cm^2 (FTO) and 0.126 cm^2 (Au-QCM sensors) respectively. The frequency of uncoated and coated QCM sensor crystals was determined with a QCM200 5 MHz measurement system (STANFORD RESEARCH SYSTEMS INC.) and an openQCM 5/10 MHz measurement system (NOVAETECH SRL). Deposited mass loadings on QCM chips were calculated according to the Sauerbrey equation[60] from determined frequency differences Δf, an overlapping electrode area A of 0.196 cm^2 and a sensitivity factor C_f of 56.6 Hz µg^{-1} cm^2 and 4.4 Hz µg^{-1} cm^2 for a 1-inch 5 and ½-inch 10 MHz AT-cut crystals respectively.

All electrochemical measurements at room temperature were carried out in a 3-electrode setup with quartz cell filled with 15 mL 0.5 M KOH (SIGMA-ALDRICH, volumetric solution) as electrolyte, using an PGSTAT302N potentiostat/galvanostat (METROHM AUTOLAB B.V.) equipped with a FRA32 M impedance analyzer connected to a Hg/HgO (0.5M KOH) reference electrode. To convert all potentials measured against Hg/HgO (0.5 M KOH) reference electrode and to ensure stability of the potential before and after every measurement session, the potential was measured against a reversible hydrogen electrode (RHE, HydroFlex, GASKATEL Gesellschaft für Gassysteme durch Katalyse und Elektrochemie mbH) stored in 0.5 M KOH and that was in turn verified by a self constructed Pt-wire/H_2(≈1 atm) electrode. The potential was determined to be 0.925 V, which is in accordance with literature stated values.[18]

The electrochemical activity of catalyst on FTO substrates was measured by *i*R-drop corrected linear sweep voltammetry (LSV) in a potential window of 1.1 - 1.7 V vs. RHE in 20 scan cycles with a scan rate of 10 mV s^{-1}. Impedance spectroscopy data at 1.0 V vs. RHE were recorded prior to each measurement to determine the corresponding electrolyte resistance (95 %) from the high frequency region. The compensated resistance was typically in the range of 18-20 Ω. Nickel hydroxide mass-based catalyst activity was either directly calculated with the measured QCM determined mass loadings (of an equal drop-cast volume) or calculated from the coating volume (3-15 µl) of a dispersion of known concentration (2 mg ml^{-1}). Current densities were determined from the mean value of capacity current corrected (mean current in potential region 1.0-1.23 V vs. RHE) anodic and cathodic scans of the respective LSV cycle.

ASSOCIATED CONTENT

Experimental details, XRD, SEM, TEM, TGA/DSC, mass-based activities at different overpotentials, cyclic voltammetry measurements.

This material is available free of charge via the Internet at http://pubs.acs.org

AUTHOR INFORMATION

Corresponding Author*

Phone: +49 2461 61 85051. E-Mail: d.fattakhova@fz-juelich.de, bein@lmu.de

Author Contributions

The manuscript was written through contributions of all authors. All authors have given approval to the final version of the manuscript.

Funding Sources

BMBF Kopernikus Project: P2X: Flexible use of renewable resources – research, validation and implementation of ‘Power-to-X’ concepts
DFG SPP1613 Solar-H2
SolTech
UMWELTnanoTECH
e-conversion (DFG Cluster of Excellence)

Notes

The authors declare no competing financial interest.

ACKNOWLEDGMENT

The authors gratefully acknowledge funding from the German Federal Ministry of Education and Research (BMBF) within the Kopernikus Project P2X: Flexible use of renewable resources – research, validation and implementation of ‘Power-to-X’ concepts. Furthermore, the authors thank the German Research Foundation (DFG SPP1613, Solar-H2 program), the e-conversion Cluster of Excellence (DFG), the research networks “Solar Technologies Go Hybrid”, UMWELTnanoTECH (State of Bavaria) and the Center for NanoScience (CeNS) for financial support. Part of the transmission electron microscope images were recorded by Steffen Schmidt (LMU chemistry department, electron microscopy unit).

ABBREVIATIONS

OER, oxygen evolution reaction; QCM, quartz crystal microbalance; EELS, electron energy loss spectroscopy; FTO, fluorine doped tin oxide;

REFERENCES

1. Parra, D.; Valverde, L.; Pino, F. J.; Patel, M. K., A review on the role, cost and value of hydrogen energy systems for deep decarbonisation. *Renew. Sust. Energ. Rev.* **2019,** *101*, 279-294.
2. Boretti, A., Renewable hydrogen to recycle CO2 to methanol. *Int. J. Hydrogen Energ.* **2013,** *38* (4), 1806-1812.
3. Kushnir, D.; Hansen, T.; Vogl, V.; Åhman, M., Adopting hydrogen direct reduction for the Swedish steel industry: A technological innovation system (TIS) study. *J. Clean. Prod.* **2020,** *242*, 118185.
4. Bazzanella, A. M.; Ausfelder, F., Low carbon energy and feedstock for the European chemical industry., Report, DECHEMA Gesellschaft für Chemische Technik und Biotechnologie e.V., Frankfurt am Main, Germany, **2017** (ISBN 978-3-89746-196-2)
5. Subbaraman, R.; Tripkovic, D.; Chang, K.-C.; Strmcnik, D.; Paulikas, A. P.; Hirunsit, P.; Chan, M.; Greeley, J.; Stamenkovic, V.; Markovic, N. M., Trends in activity for the water electrolyser reactions on 3d M(Ni,Co,Fe,Mn) hydr(oxy)oxide catalysts. *Nat. Mater.* **2012,** *11* (6), 550-557.
6. Steen, B.; Borg, G., An estimation of the cost of sustainable production of metal concentrates from the earth's crust. *Ecol. Econ.* **2002,** *42* (3), 401-413.
7. Hu, C.; Zhang, L.; Gong, J., Recent progress made in the mechanism comprehension and design of electrocatalysts for alkaline water splitting. *Energ. Environ. Sci.* **2019,** *12* (9), 2620-2645.
8. Fan, K.; Chen, H.; Ji, Y.; Huang, H.; Claesson, P. M.; Daniel, Q.; Philippe, B.; Rensmo, H.; Li, F.; Luo, Y.; Sun, L., Nickel–vanadium monolayer double hydroxide for efficient electrochemical water oxidation. *Nat. Commun.* **2016,** *7* (1), 11981.
9. Ma, W.; Ma, R.; Wang, C.; Liang, J.; Liu, X.; Zhou, K.; Sasaki, T., A Superlattice of Alternately Stacked Ni–Fe Hydroxide Nanosheets and Graphene for Efficient Splitting of Water. *ACS Nano* **2015,** *9* (2), 1977-1984.
10. Cai, Z.; Bu, X.; Wang, P.; Ho, J. C.; Yang, J.; Wang, X., Recent advances in layered double hydroxide electrocatalysts for the oxygen evolution reaction. *J. Mater. Chem. A* **2019,** *7* (10), 5069-5089.
11. You, B.; Jiang, N.; Sheng, M.; Bhushan, M. W.; Sun, Y., Hierarchically Porous Urchin-Like Ni2P Superstructures Supported on Nickel Foam as Efficient Bifunctional Electrocatalysts for Overall Water Splitting. *ACS Catal.* **2016,** *6* (2), 714-721.
12. Ledendecker, M.; Krick Calderón, S.; Papp, C.; Steinrück, H.-P.; Antonietti, M.; Shalom, M., The Synthesis of Nanostructured Ni5P4 Films and their Use as a Non-Noble Bifunctional Electrocatalyst for Full Water Splitting. *Angew. Chem. Int. Ed.* **2015,** *54* (42), 12361-12365.
13. Gao, M.; Sheng, W.; Zhuang, Z.; Fang, Q.; Gu, S.; Jiang, J.; Yan, Y., Efficient Water Oxidation Using Nanostructured α-Nickel-Hydroxide as an Electrocatalyst. *J. Am. Chem. Soc.* **2014,** *136* (19), 7077-7084.
14. Fominykh, K.; Chernev, P.; Zaharieva, I.; Sicklinger, J.; Stefanic, G.; Döblinger, M.; Müller, A.; Pokharel, A.; Böcklein, S.; Scheu, C.; Bein, T.; Fattakhova-Rohlfing, D., Iron-Doped Nickel Oxide Nanocrystals as Highly Efficient Electrocatalysts for Alkaline Water Splitting. *ACS Nano* **2015,** *9* (5), 5180-5188.
15. Vij, V.; Sultan, S.; Harzandi, A. M.; Meena, A.; Tiwari, J. N.; Lee, W.-G.; Yoon, T.; Kim, K. S., Nickel-Based Electrocatalysts for Energy-Related Applications: Oxygen Reduction, Oxygen Evolution, and Hydrogen Evolution Reactions. *ACS Catal.* **2017,** *7* (10), 7196-7225.
16. Corrigan, D. A., The Catalysis of the Oxygen Evolution Reaction by Iron Impurities in Thin Film Nickel Oxide Electrodes. *J. Electrochem. Soc.* **1987,** *134* (2), 377-384.
17. Edison, T. A. (Edison storage battery company) U.S. 876,445, **1908**.
18. Trotochaud, L.; Young, S. L.; Ranney, J. K.; Boettcher, S. W., Nickel–Iron Oxyhydroxide Oxygen-Evolution Electrocatalysts: The Role of Intentional and Incidental Iron Incorporation. *J. Am. Chem. Soc.* **2014,** *136* (18), 6744-6753.
19. Klaus, S.; Cai, Y.; Louie, M. W.; Trotochaud, L.; Bell, A. T., Effects of Fe Electrolyte Impurities on Ni(OH)2/NiOOH Structure and Oxygen Evolution Activity. *J. Phys. Chem. C* **2015,** *119* (13), 7243-7254.
20. Friebel, D.; Louie, M. W.; Bajdich, M.; Sanwald, K. E.; Cai, Y.; Wise, A. M.; Cheng, M.-J.; Sokaras, D.; Weng, T.-C.; Alonso-Mori, R.; Davis, R. C.; Bargar, J. R.; Nørskov, J. K.; Nilsson, A.; Bell, A. T., Identification of Highly Active Fe Sites in (Ni,Fe)OOH for Electrocatalytic Water Splitting. *J. Am. Chem. Soc.* **2015,** *137* (3), 1305-1313.
21. Bode, H.; Dehmelt, K.; Witte, J., Zur kenntnis der nickelhydroxidelektrode—I.Über das nickel (II)-hydroxidhydrat. *Electrochim. Acta* **1966,** *11* (8), 1079-IN1.
22. Mellsop, S. R.; Gardiner, A.; Johannessen, B.; Marshall, A. T., Structure and transformation of oxy-hydroxide films on Ni anodes below and above the oxygen evolution potential in alkaline electrolytes. *Electrochim. Acta* **2015**, *168*, 356-364.
23. Hall, D. S.; Lockwood, D. J.; Poirier, S.; Bock, C.; MacDougall, B. R., Raman and Infrared Spectroscopy of α and β Phases of Thin Nickel Hydroxide Films Electrochemically Formed on Nickel. *J. Phys. Chem. A* **2012,** *116* (25), 6771-6784.
24. Hall, D. S.; Lockwood, D. J.; Poirier, S.; Bock, C.; MacDougall, B. R., Applications of in Situ Raman Spectroscopy for Identifying Nickel Hydroxide Materials and Surface Layers during Chemical Aging. *ACS Appl. Mater. Inter.* **2014,** *6* (5), 3141-3149.
25. Chen, H.; Wang, J. M.; Pan, T.; Zhao, Y. L.; Zhang, J. Q.; Cao, C. N., The structure and electrochemical performance of spherical Al-substituted α-Ni(OH)2 for alkaline rechargeable batteries. *J. Power Sources* **2005,** *143* (1), 243-255.
26. Zhao, Y. L.; Wang, J. M.; Chen, H.; Pan, T.; Zhang, J. Q.; Cao, C. N., Al-substituted α-nickel hydroxide prepared by homogeneous precipitation method with urea. *Int. J. Hydrogen Energ.* **2004,** *29* (8), 889-896.
27. Li, P.; Duan, X.; Kuang, Y.; Li, Y.; Zhang, G.; Liu, W.; Sun, X., Tuning Electronic Structure of NiFe Layered Double Hydroxides with Vanadium Doping toward High Efficient Electrocatalytic Water Oxidation. *Adv. Energy Mater.* **2018,** *8* (15), 1703341.
28. Zand, Z.; Salimi, P.; Mohammadi, M. R.; Bagheri, R.; Chernev, P.; Song, Z.; Dau, H.; Görlin, M.; Najafpour, M. M., Nickel–Vanadium Layered Double Hydroxide under Water-Oxidation Reaction: New Findings and Challenges. *ACS Sustainable Chem. Eng.* **2019,** *7* (20), 17252-17262.
29. Jiang, J.; Sun, F.; Zhou, S.; Hu, W.; Zhang, H.; Dong, J.; Jiang, Z.; Zhao, J.; Li, J.; Yan, W.; Wang, M., Atomic-level insight into super-efficient electrocatalytic oxygen evolution on iron and vanadium co-doped nickel (oxy)hydroxide. *Nat. Commun.* **2018,** *9* (1), 2885.
30. Gonçalves, J. M.; da Silva, M. I.; Angnes, L.; Araki, K., Vanadium-containing electro and photocatalysts for the oxygen evolution reaction: a review. *J. Mater. Chem. A* ***2020,*** *8, 2171-2206.*
31. Wang, R.; Lang, J.; Liu, Y.; Lin, Z.; Yan, X., Ultra-small, size-controlled Ni(OH)2 nanoparticles: elucidating the relationship between particle size and electrochemical performance for advanced energy storage devices. *NPG Asia Mater.* **2015,** *7*, e183.
32. Fominykh, K.; Feckl, J. M.; Sicklinger, J.; Döblinger, M.; Böcklein, S.; Ziegler, J.; Peter, L.; Rathousky, J.; Scheidt, E.-W.; Bein, T.; Fattakhova-Rohlfing, D., Ultrasmall Dispersible Crystalline Nickel Oxide Nanoparticles as High-Performance Catalysts for Electrochemical Water Splitting. *Adv. Funct. Mater.* **2014,** *24* (21), 3123-3129.
33. Reier, T.; Oezaslan, M.; Strasser, P., Electrocatalytic Oxygen Evolution Reaction (OER) on Ru, Ir, and Pt Catalysts: A Comparative Study of Nanoparticles and Bulk Materials. *ACS Catal.* **2012,** *2* (8), 1765-1772.
34. Tessier, C.; Haumesser, P. H.; Bernard, P.; Delmas, C., The Structure of Ni (OH) 2: From the Ideal Material to the Electrochemically Active One. *J. Electrochem. Soc.* **1999,** *146* (6), 2059-2067.
35. Delmas, C.; Tessier, C., Stacking faults in the structure of nickel hydroxide: a rationale of its high electrochemical activity. *J. Mater. Chem.* **1997,** *7* (8), 1439-1443.
36. Xu, L.; Ding, Y.-S.; Chen, C.-H.; Zhao, L.; Rimkus, C.; Joesten, R.; Suib, S. L., 3D Flowerlike α-Nickel Hydroxide with Enhanced Electrochemical Activity Synthesized by Microwave-Assisted Hydrothermal Method. *Chem. Mater.* **2008,** *20* (1), 308-316.

37. Zhang, Q.; Zhang, C.; Liang, J.; Yin, P.; Tian, Y., Orthorhombic α-NiOOH Nanosheet Arrays: Phase Conversion and Efficient Bifunctional Electrocatalysts for Full Water Splitting. *ACS Sustain. Chem. Eng.* **2017,** *5* (5), 3808-3818.

38. Luan, C.; Liu, G.; Liu, Y.; Yu, L.; Wang, Y.; Xiao, Y.; Qiao, H.; Dai, X.; Zhang, X., Structure Effects of 2D Materials on α-Nickel Hydroxide for Oxygen Evolution Reaction. *ACS Nano* **2018,** *12* (4), 3875-3885.

39. Sutto, T. E., One-Step Bulk Synthesis of Stable, Near Unit-Cell Sized Oxide Nanoparticles and Nanoparticle Blends Using KO2. *Inorg. Chem.* **2014,** *53* (9), 4570-4578.

40. Tessier, C.; Guerlou-Demourgues, L.; Faure, C.; Basterreix, M. t.; Nabias, G.; Delmas, C., Structural and textural evolution of zinc-substituted nickel hydroxide electrode materials upon ageing in KOH and upon redox cycling. *Solid State Ionics* **2000,** *133* (1–2), 11-23.

41. Bernard, M. C.; Bernard, P.; Keddam, M.; Senyarich, S.; Takenouti, H., Characterisation of new nickel hydroxides during the transformation of α Ni(OH)2 to β Ni(OH)2 by ageing. *Electrochim. Acta* **1996,** *41* (1), 91-93.

42. Briggs, G. W. D.; Stott, G. W.; Wynne-Jones, W. F. K., The nickel hydroxide electrode; the effect of ageing—II. Changes in electrochemical behaviour. *Electrochim. Acta* **1962,** *7* (3), 249-256.

43. Visscher, W.; Barendrecht, E., Investigation of thin-film α- and β-Ni(OH)2 electrodes in alkaline solutions. *J. Electroanal. Chem.* **1983,** *154* (1), 69-80.

44. Jung, S. C.; Sim, S. L.; Soon, Y. W.; Lim, C. M.; Hing, P.; Jennings, J. R., Synthesis of nanostructuredβ-Ni(OH)2by electrochemical dissolution–precipitation and its application as a water oxidation catalyst. *Nanotechnology* **2016,** *27* (27), 275401.

45. Shannon, R., Revised effective ionic radii and systematic studies of interatomic distances in halides and chalcogenides. *Acta Crystallogr. A* **1976,** *32* (5), 751-767.

46. Bhuvaneswari, M. S.; Selvasekarapandian, S.; Kamishima, O.; Kawamura, J.; Hattori, T., Vibrational analysis of lithium nickel vanadate. *J. Power Sources* **2005,** *139* (1), 279-283.

47. Schreckenbach, J. P.; Witke, K.; Butte, D.; Marx, G., Characterization of thin metastable vanadium oxide films by Raman spectroscopy. *Fresenius' J. Anal. Chem.* **1999,** *363* (2), 211-214.

48. Park, H. W.; Chae, J. S.; Park, S.-M.; Kim, K.-B.; Roh, K. C., Nickel-based layered double hydroxide from guest vanadium oxide anions. *Met. Mater. Int.* **2013,** *19* (4), 887-894.

49. Zhang, S.; Diehl, L.; Wrede, S.; Lotsch, B.V.; Scheu, C. Structural Evolution of Ni-Based Co-Catalysts on $[Ca_2Nb_3O_{10}]^-$ Nanosheets during Heating and Their Photocatalytic Properties. *Catalysts* **2020**, *10*, 13.

50. Li, K.; Xue, D., Estimation of Electronegativity Values of Elements in Different Valence States. *J. Phys. Chem. A* **2006,** *110* (39), 11332-11337.

51. Lyons, M. E. G.; Doyle, R. L.; Godwin, I.; O'Brien, M.; Russell, L., Hydrous Nickel Oxide: Redox Switching and the Oxygen Evolution Reaction in Aqueous Alkaline Solution. *J. Electrochem. Soc.* **2012,** *159* (12), H932-H944.

52. Yeo, B. S.; Bell, A. T., In Situ Raman Study of Nickel Oxide and Gold-Supported Nickel Oxide Catalysts for the Electrochemical Evolution of Oxygen. *J. Phys. Chem. C* **2012,** *116* (15), 8394-8400.

53. Liang, X.; Xiao, J.; Gou, Y.; Chen, B., Synthesis and catalysis properties of NiO flower-like spheres and nanosheets: Water-induced phase transformation of nickel hydroxides. *J. Mater. Res.* **2011,** *26* (24), 3091-3097.

54. Liang, Z.-H.; Zhu, Y.-J.; Hu, X.-L., β-Nickel Hydroxide Nanosheets and Their Thermal Decomposition to Nickel Oxide Nanosheets. *J. Phys. Chem. B* **2004,** *108* (11), 3488-3491.

55. Sato, T.; Nakamura, T.; Ozawa, F., Thermal decomposition of nickel hydroxide. *J. Appl. Chem. Biotechn.* **1975,** *25* (8), 583-590.

56. Xing, W.; Li, F.; Yan, Z.-f.; Lu, G. Q., Synthesis and electrochemical properties of mesoporous nickel oxide. *J. Power Sources* **2004,** *134* (2), 324-330.

57. Park, H. W.; Na, B.-K.; Cho, B. W.; Park, S.-M.; Roh, K. C., Influence of vanadium doping on the electrochemical performance of nickel oxide in supercapacitors. *Phys. Chem. Chem. Phys.* **2013,** *15* (40), 17626-17635.

58. Le Bihan, S.; Figlarz, M., Croissance de l'hydroxyde de nickel Ni(OH)2 à partir d'un hydroxyde de nickel turbostratique. *J. Cryst. Growth* **1972,** *13-14*, 458-461.

59. Zhang, S.; Scheu, C., Evaluation of EELS spectrum imaging data by spectral components and factors from multivariate analysis. *Microscopy* **2017,** *67* (suppl_1), i133-i141. (doi: 10.1093/jmicro/dfx091)

60. Sauerbrey, G., Verwendung von Schwingquarzen zur Wägung dünner Schichten und zur Mikrowägung. *Z. Phys.* **1959,** *155* (2), 206-222.

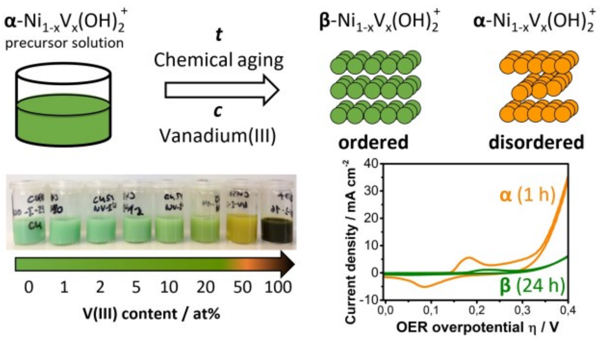

ToC image: Schematic illustration of the effect of vanadium(III) doping and chemical aging duration on the phase transformation of α-$Ni(OH)_2$ to well-stacked β-$Ni(OH)_2$ or remaining V(III) containing disordered α-phase. An evaluation as oxygen evolution reaction catalysts revealed a strong influence of the chemical aging process and related crystallinity with the electrocatalytic activity.